
DeltaPhi: Learning Physical Trajectory Residual for PDE Solving

Xihang Yue, Linchao Zhu, Yi Yang
 ReLER, CCAI, Zhejiang University
 {xihang, zhulinchao, yangyics}@zju.edu.cn

Abstract

Although neural operator networks theoretically approximate any operator mapping, the limited generalization capability prevents them from learning correct physical dynamics when potential data biases exist, particularly in the practical PDE solving scenario where the available data amount is restricted or the resolution is extremely low. To address this issue, we propose and formulate the Physical Trajectory Residual Learning (DeltaPhi), which learns to predict the physical residuals between the pending solved trajectory and a known similar auxiliary trajectory. First, we transform the *direct operator mapping* between input-output function fields in original training data to *residual operator mapping* between input function pairs and output function residuals. Next, we learn the surrogate model for the residual operator mapping based on existing neural operator networks. Additionally, we design helpful customized auxiliary inputs for efficient optimization. Through extensive experiments, we conclude that, compared to direct learning, physical residual learning is preferred for PDE solving.

1 Introduction

Due to lacking analytical solutions, solving complex Partial Differential Equations (PDEs), *e.g.* Navier-Stokes, relies on numerical simulation based on ultra-fine grid division, which consumes expensive computational resources and time. To resolve this, machine learning based PDE solving [1–5] has sparked extensive research interest in recent years. Notably, the operator learning [6, 2, 1] directly learns the mapping between the input-output function fields, forming a surrogate model for a given parametric PDE. Then the solution for any input functions could be quickly obtained via neural network forward computation.

Despite current operator learning networks [2, 3] theoretically being able to approximate any operator mapping, their generalization capabilities remain limited. First, the networks are prone to overfitting to training resolution while suffering performance degradation on other resolutions [7], especially when the training resolution is extremely low. Second, when available training data is limited, the network may struggle to accurately model the correct physical dynamics due to potential biases in the data. Third, data scarcity and bias are common occurrences in practical PDE solving [8, 9]. Therefore, further investigation is required to enhance the neural operator generalization ability.

In this work, for generalized PDE solving, we introduce the *Physical Trajectory Residual Learning* (DeltaPhi), which reformulates the *direct operator mapping* between the input-output function fields as the mapping between input function pairs and output function residuals (*residual operator mapping*). The residual operator mapping could be learned with any existing neural operators (such as FNO [2], NORM [10], FFNO [11], *etc.*), thereby obtaining corresponding *residual neural operator*. First, we reconstruct the training set from data pairs of direct operator mapping to data pairs of residual operator mapping, via assigning an auxiliary trajectory to every training data. The auxiliary trajectory is a different trajectory sampled from the training set based on *similar trajectory retrieval*.

Next, we optimize the neural operator network with reconstructed training data. By concatenating the pending solved input function and auxiliary trajectory together as input of the network, and adding the auxiliary trajectory solution to the final output of the network via residual connection, we could optimize the network with existing training frameworks. All other setups (including the loss function, trainable weights amount, *etc.*) remain consistent with the base operator networks. Compared to previous direct operator learning, the reconstructed residual training labels could be customized with enhanced diversity through selecting appropriate auxiliary samples. Consequently, the restricted diversity and potential distribution bias due to limited training data amount could be mitigated, thereby obtaining more generalized surrogate models.

Residual learning methodology has been extensively studied in the machine learning community [12–15]. Previous works present various benefits derived from residual learning, such as enhancing generalization capability, handling complex regression mapping, *etc.* In this work, we introduce this concept into the neural operator learning task, a more complex regression task involving learning the mapping between high-dimension (tens of thousands) fields. The residuals between different but similar physical trajectories are learned, and utilized to solve PDEs. Through the visualization analysis of label distribution, we statistically validate the favorable generalization property of learning the residual operator mapping.

The contributions are summarized as follows:

- We propose and formulate a novel framework for data-driven PDE solving in restricted data (limited amount, low resolution, biased distribution) scenarios, *i.e.* the Physical Trajectory Residual Learning (DeltaPhi).
- We statistically analysis the advantage of residual operator learning and make instantiations based on similar trajectory retrieval and existing neural operator networks.
- We validate the superiority of residual operator learning through extensive experiments across different PDE problems, different physical domains (both regular and irregular problems), different base models, different training set sizes, and different training resolutions. Additionally, detailed ablation studies are conduct.

2 Related Work

Neural operator learning. Fourier Neural Operator (FNO) [2] utilizes the Fourier Transform based integral operation to efficiently learn the physical dynamics using limited training data. Factorized Fourier Neural Operator (FFNO) [11] factorize the Fourier Transform along each dimension, reducing the number of network weights. Clifford Fourier Neural Operator (CFNO) [16] employs the Clifford Algebra in the network architecture, incorporating geometry prior between multi physical fields. The various neural operators could be simply integrated with the proposed Physical Trajectory Residual Learning.

Other works investigate architecture improvements for different needs, including chaotic systems modeling [17], physical-informed instance-wise finetuning [7], accelerating computation [18–20], spherical fields processing [21], irregular fields learning [22, 23], non-periodic boundary fields modeling [24], large-scale pretraining [25, 26], *etc.* In addition, some works explore other network backbones, *e.g.* improved frequency-spatial domain transformation [27–30], convolutions [31], graph neural network [32, 6, 33], attention mechanism [34, 23, 35], and diffusion models [36]. Incorporating residual learning with these designs is worth exploring in the future.

Residual learning in previous works. Some works learn residual between different data samples. Similar to ResMem [12], we also utilize the training set as auxiliary memory during inference, enjoying its generalization enhancement property. The difference lies that (1) we memorize the auxiliary labels and learn the residuals, while ResMem memorizes the residuals and learns the labels, (2) our framework is end-to-end trained while ResMem is trained in separate stages. Similar external memory augmented strategies are popular in the Language Modeling community [37, 38].

Other works learn residuals between low resolution and high resolution representation for image super-resolution [39] and deep learning based CFD simulation [39]. Similar residual learning is investigated in time series prediction task [40, 13]. The primary distinction between these works to ours is that we do not utilize the corresponding low-resolution solutions or previous time-step solutions, but instead, learn the residuals between different trajectories.

3 Methodology

3.1 Preliminary

3.1.1 Direct learning formulation

Direct operator mapping. Previous works [2, 11, 23] formulate the parametric PDE numerical solution as an operator mapping between two infinite dimensional function spaces:

$$\mathcal{G} : \mathcal{A} \longrightarrow \mathcal{U}, \quad (1)$$

where \mathcal{A} and \mathcal{U} are both banach spaces of functions. For steady-state solving problems, *e.g.* Darcy Flow, $a(x) \in \mathcal{A}$ represents the diffusion coefficient function, and $u(x) \in \mathcal{U}$ is the corresponding solution function. For time-series forecasting problems, *e.g.* Navier-Stokes, $a(x) \in \mathcal{A}$ typically denotes the state function of the preceding few steps, while $u(x) \in \mathcal{U}$ represents the function in the subsequent few steps. The learning task is to study a parameterized surrogate model \mathcal{G}_θ for \mathcal{G} .

Domain discretization. Following [2, 41], we numerically process the function $a(x)$ and $u(x)$ by taking the discretization of the continuous domain. For regular domain problems, we uniformly discretize the regular field, using standard rectangular grids to capture the physical states. For irregular domain problems, we take the discrete mesh representation of the field.

Optimization problem. Consider the training set \mathcal{T} consisting of N i.i.d. pairs $\{a_i, u_i\}_{i=1}^N$, where $a_i \in \mathcal{A}$, $u_i \in \mathcal{U}$, the objective is to find θ that minimizes the following cost function:

$$\ell = \sum_{i=1}^N \mathcal{L}(\mathcal{G}_\theta(a_i), u_i), \quad (2)$$

where \mathcal{L} is a cost function that measures the difference between two functions. During inference, given the input function $a \in \mathcal{A}$, we obtain the corresponding solution $u = \mathcal{G}_\theta(a)$.

3.1.2 Neural Operator Network

Prior works [2, 34, 11] have extensively explored neural network architectures for learning the operator mapping \mathcal{G}_θ between function spaces. Among these, the Fourier Neural Operator (FNO) [2, 1] has been the most commonly applied model across various physical systems. Neural operators are defined as multi-layer networks formulated as follows:

$$\mathcal{G}_\theta = Q \circ \sigma(W_l + \mathcal{K}_l) \circ \cdots \circ \sigma(W_i + \mathcal{K}_i) \circ \cdots \circ \sigma(W_1 + \mathcal{K}_1) \circ P, \quad (3)$$

where l represents the number of layers in the network. The projector P encodes the input function a_i into an implicit embedding v_0 . The operators W_i and \mathcal{K}_i at the i -th layer transform the input function v_{i-1} into v_i . σ is an element-wise non-linear operation introduced for learning non-linear mapping between function spaces. Q is the output projector which decodes the last layer's output $v_l(x)$ into the targeted function $u_i(x)$.

The components of \mathcal{G}_θ could be differently instantiated across various models. Typically, P and Q are implemented as fully connected layers. In Fourier Neural Operator [2], \mathcal{K}_i is instantiated as an integral operator based on Fourier Transform, and W_i is a linear fully connected layer. In NORM [10], \mathcal{K}_i is implemented based on the Laplacian Transform for processing irregular domains. In addition, \mathcal{K}_i can also be a convolution operation, adopting an architecture similar to Resnet [42].

Although direct operator learning networks can theoretically approximate any operator mapping, they encounter limited generalization capabilities in practical applications. First, the networks tend to overfit on trained resolution, and suffer performance drops on high resolution inference. Second, the model is vulnerable to potential bias in training data (especially when the data amount is limited), thus failing to capture the intrinsic physical trajectory dynamics.

3.2 Physical Trajectory Residual Learning

3.2.1 Formulation

Different from the aforementioned direct operator learning, we propose to learn the *residual operator mapping* that captures the differences between pairs of physical trajectories:

$$\begin{aligned} \mathcal{G}^\Delta : \mathcal{A}^2 &\longrightarrow \Delta\mathcal{U}, \\ \mathcal{A}^2 &: \{(a_i, a_j) \mid a_i \in \mathcal{A}, a_j \in \mathcal{A}\}, \\ \Delta\mathcal{U} &: \{u_i - u_j \mid u_i \in \mathcal{U}, u_j \in \mathcal{U}\}, \end{aligned} \quad (4)$$

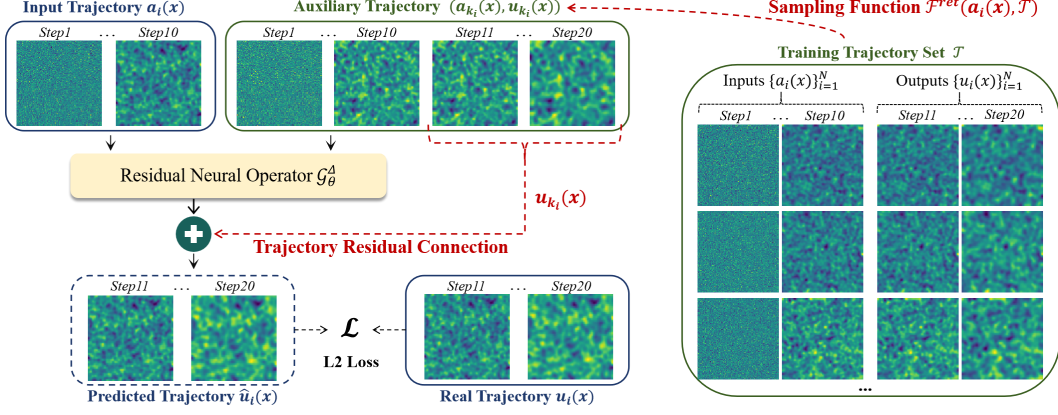


Figure 1: The overall architecture of Physical Trajectory Residual Learning. Given an *input trajectory* a_i , we first sample a similar *auxiliary trajectory* (a_{k_i}, u_{k_i}) from the *training trajectory set* \mathcal{T} . Subsequently, the trajectory a_i and (a_{k_i}, u_{k_i}) are concatenated and fed into the the neural operator $\mathcal{G}_\theta^\Delta$, producing the *predicted trajectory residual*. Finally, the predicted solution \hat{u}_i is obtained by adding the *predicted trajectory residual* with the auxiliary solution u_{k_i} .

where \mathcal{G}^Δ represents the residual mapping operator. \mathcal{A}^2 is the Cartesian product of \mathcal{A} with itself, meaning it consists of all possible pairs of functions from \mathcal{A} . $\Delta\mathcal{U}$ represents the space of function residuals, which are the differences between pairs of functions from \mathcal{U} . a_* and u_* are functions in the space of \mathcal{A} and \mathcal{U} , respectively.

The residual mapping operator \mathcal{G}^Δ maps the input functions pair (a_i, a_j) into the corresponding function residual $u_i - u_j$, i.e. $u_i - u_j = \mathcal{G}^\Delta(a_i, a_j)$. This approach leverages the concept of residuals to simplify the learning task. Instead of learning the direct operator mapping from \mathcal{A} to \mathcal{U} , we focus on learning the differences between output functions. The transformed training label distribution, i.e. the function residual distribution, could have sufficient diversity by selecting appropriate auxiliary samples, thereby alleviating the training data bias and better handling the unknown function to be solved. We detail the explanation about this in Section 3.2.5.

Both direct operator mapping and residual operator mapping are mappings between Banach spaces of functions. Therefore, we could employ the off-the-shelf neural operator networks [2, 11] as the base network backbone. Neural operator networks are designed to handle mapping between function spaces and are known for their universal approximation capabilities, making them well-suited for residual operator mapping.

3.2.2 Auxiliary Trajectory Sampling

Given an input function (or named as input trajectory) a_i , we need an auxiliary trajectory (a_{k_i}, u_{k_i}) to learn the residual neural operator \mathcal{G}^Δ and infer the corresponding output u_i of a_i . The auxiliary trajectory can be sampled from the existing data, allowing us to leverage prior knowledge to improve the generalization capabilities of the model. By selecting an appropriate auxiliary trajectory, we can simplify the computation and enhance the robustness of the residual operator mapping.

Given the training set $\mathcal{T} = \{a_i, u_i\}_{i=1}^N$, each data pair (a_i, u_i) is associated with an auxiliary trajectory (a_{k_i}, u_{k_i}) , sampled from \mathcal{T} . The index k_i of the auxiliary trajectory is defined by:

$$k_i = \mathcal{F}^{ret}(a_i, \mathcal{T}), k_i \in \{1, 2, \dots, N\}, k_i \neq i, \quad (5)$$

where \mathcal{F}^{ret} is the sampling function. A straightforward implementation of \mathcal{F}^{ret} could be random sampling from $\{1, 2, \dots, i-1, i+1, \dots, N\}$. Using the calculated k_i , we transform the origin training set \mathcal{T} to a residual training set $\mathcal{T}^{res} = \{(a_i, a_{k_i}), u_i - u_{k_i}\}_{i=1}^N$. Below we present our implementation of \mathcal{F}^{ret} in detail.

Training stage. During training, give an input function a_i , we randomly sample a trajectory a_j from the set of trajectories with top-k similarity scores to a_i . The sampling function \mathcal{F}^{ret} is defined as:

$$\begin{aligned} \mathcal{F}^{ret}(a_i, \mathcal{T}) &= \text{RandSample}(\text{argtopK}_{j, j \neq i} \text{Sim}(a_i, a_j)), \\ \text{Sim}(a_i, a_j) &= 1 - \frac{a_i \cdot a_j}{\|a_i\| \|a_j\|}, \end{aligned} \quad (6)$$

where $\text{RandSample}(\cdot)$ represents randomly sampling one element from the given set. K is the sampling range, a hyperparameter that could be adjusted for different PDEs. For a fair comparison, except for specific statements, we set $K = 20$ for all experiments in this work.

Inference stage. During inference, given the input function a^{test} , we select the most similar auxiliary trajectory from the training set:

$$\mathcal{F}^{ret}(a^{test}, \mathcal{T}) = \text{argmax}_j \text{Sim}(a^{test}, a_j). \quad (7)$$

We empirically found the model performance is robust to the choice of auxiliary trajectories. In Appendix A.3, we experiment with randomly sampled auxiliary trajectories from the top ten similarity scores and find the standard deviation across five repeating evaluations is quite small. This indicates that the residual neural operator effectively learns the residual operator mapping for the same a_i with varied auxiliary trajectories. We further present the trajectory sampling for varied resolution fields in Appendix C.3. Appendix C.4 provides the cost analysis of the trajectory sampling.

3.2.3 Auxiliary Trajectory Integration

As aforementioned, the residual operator \mathcal{G}^Δ requires additional auxiliary function a_{k_i} as input. In specific implementation, a_i and a_{k_i} could be straightly concatenated along their channel dimension:

$$a_{input} = a_i \oplus a_{k_i}, \quad (8)$$

where \oplus represents the concatenation operation of two vectors. Then the concatenated vector a_{input} is feeded into the neural operator network:

$$v_0 = P(a_{input}), \quad (9)$$

where P is the fully connected encoder in the operator network (Equation (3)), and v_0 represents the first latent function in the hidden space.

Integration of auxiliary trajectory with variant resolution. In cases where the auxiliary input function a_{k_i} has a different resolution from the input function a_i , we address this discrepancy via field interpolation techniques. We present the details in Appendix C.2.

Integration of auxiliary trajectory with additional related information. The residual operator mapping can be challenging to learn due to the variability of output residuals for different auxiliary samples. To mitigate such difficulty, we introduce additional information related to a_{k_i} as inputs for residual neural operators:

- For time-series PDE solving, *e.g.* Navier-Stokes, we only input the last few time steps of a_{k_i} .
- We use the corresponding $u_{k_i}(x)$ of $a_{k_i}(x)$ as the input.
- We utilize calculated relation metrics, *e.g.* similarity between a_i and a_{k_i} , as inputs.

Our experimental results (Appendix A.2) indicate that this customized input strategy indeed improves the performance of residual neural operators.

3.2.4 Residual Operator Learning

To train the parameterized surrogate model $\mathcal{G}_\theta^\Delta$ of \mathcal{G}^Δ using the residual training set \mathcal{T}^{res} , we formulate the following optimization problem to determine the optimal parameter by minimizing the cost function:

$$\ell = \sum_{i=1}^N \mathcal{L}(\mathcal{G}_\theta^\Delta(a_i, a_{k_i}), u_i - u_{k_i}), \quad (10)$$

where \mathcal{L} is the cost function for assessing the discrepancy between function residuals.

The optimization of the physical trajectory residual depicted in Equation (10) can be effectively implemented using existing learning frameworks [2, 11]. This involves introducing a *trajectory residual connection* on the explicit output of the base operator network. Specifically, we add the auxiliary solution u_{k_i} to the predicted residual from the final output of the operator network:

$$\hat{u}_i = Q(v_l) + u_{k_i}, \quad (11)$$

where Q is the last fully connected projector of the operator network, v_l is the last latent function in hidden space produced by $\sigma(W_l + \mathcal{K}_l)$ shown in Equation (3).

During inference, given input function a^{test} , we select the auxiliary trajectory $(a_{k_t}(x), u_{k_t}(x))$ from the training set \mathcal{T} using the sampling function \mathcal{F}^{ret} .

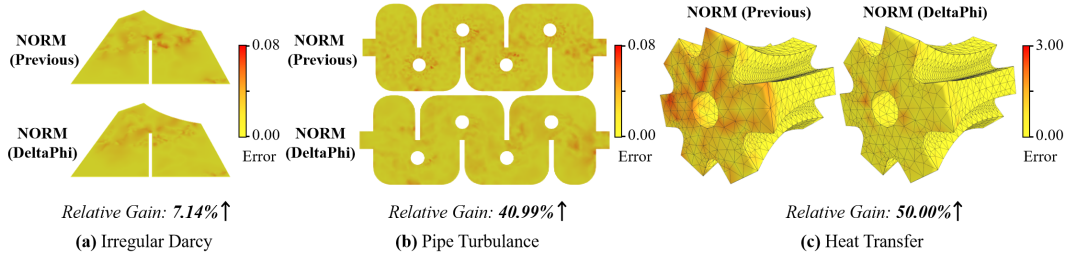


Figure 2: Prediction error visualization on irregular domain problems.

3.2.5 Discussion

Compared to direct operator learning, residual operator learning presents the following advantages.

Mitigation of distribution bias. Residual operator learning allows us to control the training label distribution, thereby mitigating the data distribution bias. We posit that the similarity between input functions and the corresponding output functions' similarity are positively correlated. This correlation is validated empirically in non-chaotic systems, as demonstrated in Darcy Flow experiments (Figure 4). Consequently, the distribution of label residuals can be effectively controlled by adjusting the selection range (K in Equation (6)) of the sampling function \mathcal{F}^{ret} . This adjustment allows the construction of sufficiently diverse training labels, thereby alleviating distribution bias in restricted data scenarios and enhancing the generalization capabilities of neural operators.

Prevent overfitting. In scenarios with limited training data, neural networks tend to memorize the training set, leading to significant overfitting. Residual learning effectively addresses this issue by modifying the training labels through the use of various auxiliary samples in each training epoch, thus reducing the risk of overfitting.

Incorporation of explicit physical priors. The auxiliary sample acts as a non-parametric physical prior. As shown in previous work [12], involving external memory components benefits the model's generalization capability. Moreover, the explicit external memory allows specific needs during inference, such as handling boundary conditions and high resolution samples.

4 Experiment

This section provides the experiments on various PDEs, resolution generalization problem, and statistical analysis of residual operator learning. Appendix A presents additional ablation studies.

4.1 Residual Learning vs. Direct Learning on Various PDEs

This section validates residual operator learning on various PDEs. The experiment covers both irregular domain problems and regular domain problems. In addition, we test the performance improvement under variant training data amount. To ensure fair comparisons, all baselines and our counterpart models are compared with exactly same hyperparameters, trainable weight amount, optimizer configuration, and training step.

Irregular domain problems. We validate the effectiveness of the proposed approach on irregular domain problems. The experimental setup is exactly same as [10]. We experiment with five problems covering both 2D and 3D scenarios, *i.e.* Irregular Darcy Flow (2D), Pipe Turbulence (2D), Heat Transfer (3D), Composite (3D), and Blood Flow (3D), all of which are defined on irregular physical domains and processed as a set of discrete triangle meshes. The baselines contain GraphSAGE [43], DeepOnet [3], POD-DeepOnet [44], FNO [2] and NORM [10]. We implement the residual learning version of NORM and compare it with the direct learning model under exactly same setup. Appendix B presents more experimental details about the datasets and baselines.

We report the results in Table 1. The residual neural operator NORM (DeltaPhi) consistently outperforms all baselines on all irregular domain problems. The enhancement is particularly significant on Pipe Turbulence and Heat Transfer problem, with 40% - 50% relative improvement (the row "Relative Gain" in Table 1) over original NORM, *i.e.* the NORM (Previous). These results indicate that the proposed residual operator learning works well on irregular domain problems.

Table 1: Relative error comparison of operator learning on irregular domains.

| Model | Irregular Darcy (Train Size=1000) | Pipe Turbulence (Train Size=300) | Heat Transfer (Train Size=100) | Composite (Train Size=400) | Blood Flow (Train Size=400) |
|----------------------|--------------------------------------|-------------------------------------|-----------------------------------|-------------------------------|--------------------------------|
| GraphSAGE | 6.73e-2 | 2.36e-1 | - | 2.09e-1 | - |
| DeepOnet | 1.36e-2 | 9.36e-2 | 7.20e-4 | 1.88e-2 | 8.93e-1 |
| POD-DeepOnet | 1.30e-2 | 2.59e-2 | 5.70e-4 | 1.44e-2 | 3.74e-1 |
| FNO | 3.83e-2 | 3.80e-2 | - | - | - |
| NORM (Previous) | 1.05e-2 | 1.01e-2 | 2.70e-4 | 9.99e-3 | 4.82e-2 |
| NORM (DeltaPhi) | 9.75e-3 | 5.96e-3 | 1.35e-4 | 9.18e-3 | 4.29e-2 |
| Relative Gain | 7.14% ↑ | 40.99% ↑ | 50.00% ↑ | 8.11% ↑ | 11.00% ↑ |

Table 2: Relative error comparison on regular Darcy Flow and Navier-Stokes Equation.

| Model | Darcy Flow | | | Navier-Stokes Equation | | |
|----------|-------------------------------|---------------------------------|---------------|-------------------------------|---------------------------------|---------------|
| | Direct Learning (Previous) | Residual Learning (DeltaPhi) | Relative Gain | Direct Learning (Previous) | Residual Learning (DeltaPhi) | Relative Gain |
| FNO | 3.70e-2 | 3.31e-2 | 10.54% ↑ | 2.24e-1 | 2.13e-1 | 4.86% ↑ |
| FFNO | 5.22e-2 | 2.93e-2 | 43.76% ↑ | 2.40e-1 | 2.20e-1 | 8.54% ↑ |
| CFNO | 4.79e-2 | 3.15e-2 | 34.23% ↑ | 3.51e-1 | 3.35e-1 | 4.56% ↑ |
| GNOT | 6.74e-2 | 5.50e-2 | 18.39% ↑ | 4.16e-1 | 4.06e-1 | 2.33% ↑ |
| Galerkin | 6.78e-2 | 6.54e-2 | 3.60% ↑ | 3.60e-1 | 3.54e-1 | 1.86% ↑ |
| MiOnet | 8.61e-2 | 8.22e-2 | 4.53% ↑ | 4.79e-1 | 4.61e-1 | 3.80% ↑ |
| Resnet | 1.25e-1 | 1.07e-1 | 14.14% ↑ | 4.39e-1 | 4.30e-1 | 1.87% ↑ |

In addition, we visualize the prediction error in Figure 2. The error value is calculated as the absolute difference between the predicted function \hat{u} and ground-truth function u^{GT} , *i.e.* $|\hat{u} - u^{GT}|$. Compared to previous direct learning methods, DeltaPhi significantly reduces the error scale.

Regular domain problems. We conduct the experiment on two regular domain problems *i.e.* Darcy Flow and Navier-Stokes, following [2]. The training data amount is 100. We validate DeltaPhi on different neural operators, including FNO [2], FFNO [11], CFNO [16], GNOT [23], Galerkin [34], MiOnet [45] and Resnet [42]. The performance is measured with relative error. Appendix B presents more experimental details.

Table 2 presents the experimental results. On both Darcy Flow and Navier-Stokes Equations, the proposed residual operator learning (DeltaPhi) consistently improves performance across different base models. The results validate the effectiveness of DeltaPhi on regular domain problems. However, we observe that the performance improvement of the model on the Navier-Stokes Equation is relatively marginal. We conjecture this is due to the complexity of the fluid dynamic with the viscosity $\nu = 1e - 5$, whereby the correlation between input and output functions with long time intervals is diminished, *i.e.* similar initial functions $a(x)$ do not necessarily correspond to sufficiently similar output functions $u(x)$. This is a limitation of the current implementation that does not affect the conclusion of this work. It could be alleviated with additional designs such as performing auxiliary trajectory retrieval at each step of time-series prediction to mitigate the decay in correlation between input and output functions.

Different training scales. We test the residual operator learning on different training set sizes. The experiment is conducted on Darcy Flow problems, with three base models FNO, FFNO, and Resnet. Specifically, we train all models with five training data scales 100, 300, 500, 700, and 900 respectively, and evaluate their performance on the additional same 100 testing samples.

Table 3: Relative error comparison on different training scales.

| Model | Different Train Size | | | | |
|----------------------|----------------------|----------|----------|----------|----------|
| | 100 | 300 | 500 | 700 | 900 |
| FNO (Previous) | 3.70e-2 | 1.40e-2 | 1.02e-2 | 8.37e-3 | 7.39e-3 |
| FNO (DeltaPhi) | 3.31e-2 | 1.34e-2 | 9.64e-3 | 8.06e-3 | 7.18e-3 |
| Relative Gain | 10.54% ↑ | 4.08% ↑ | 5.49% ↑ | 3.74% ↑ | 2.83% ↑ |
| FFNO (Previous) | 5.22e-2 | 1.69e-2 | 9.73e-3 | 7.48e-3 | 6.16e-3 |
| FFNO (DeltaPhi) | 2.93e-2 | 1.11e-2 | 7.20e-3 | 6.22e-3 | 5.30e-3 |
| Relative Gain | 43.76% ↑ | 34.47% ↑ | 25.98% ↑ | 16.79% ↑ | 14.02% ↑ |
| Resnet (Previous) | 1.25e-1 | 1.22e-1 | 1.21e-1 | 1.21e-1 | 1.21e-1 |
| Resnet (DeltaPhi) | 1.07e-1 | 9.42e-2 | 9.08e-2 | 8.63e-2 | 8.31e-2 |
| Relative Gain | 14.14% ↑ | 22.74% ↑ | 25.14% ↑ | 28.92% ↑ | 31.51% ↑ |

The experimental results are shown in Table 3. On different training set sizes, DeltaPhi improves the prediction performances of neural operators. As the number of available training data decreases, the relative improvement percent (the row "Relative Gain") consistently increases on FNO and FFNO. In addition, several residual neural operators even outperform direct neural operators using less training data amount, *e.g.* FFNO (DeltaPhi) with training size 500 outperforms FFNO (Previous) with training size 700,

Resnet (DeltaPhi) with training size 700 outperforms Resnet (Previous) with training size 900. The experimental results empirically demonstrate the effectiveness of DeltaPhi across different training set scales.

4.2 Residual Learning vs. Direct Learning on Resolution Generalization Problem

This section presents the experimental results of training-free resolution generalization.

Resolution generalization problem. Fourier neural operator [2] enables zero-shot resolution generalization inference. However, when the training data grid is excessively coarse, the inference performance over high resolution data drops a lot. The performance degeneration is more serious when learning operator mapping between fields with weaker spatial continuity such as Darcy Flow.

Setup. We conduct the training-free resolution generalization experiment on Darcy Flow [2]. Specifically, we train the models with low resolutions 85×85 , 43×43 , 31×31 , and 22×22 respectively, then evaluate them using high resolution 421×421 test data. Both FNO [2] and FFNO [11] are compared as the base models. The training set scale includes 100 and 900 trajectories.

Table 4: Relative error comparison on zero-shot resolution generalization.

| Model | Train Size=100 | | | | Train Size=900 | | | |
|----------------------|----------------|----------------|----------------|----------------|----------------|----------------|----------------|----------------|
| | 85×85 | 43×43 | 31×31 | 22×22 | 85×85 | 43×43 | 31×31 | 22×22 |
| FNO (Previous) | 7.29e-2 | 1.19e-1 | 1.49e-1 | 1.70e-1 | 6.73e-2 | 1.11e-1 | 1.34e-1 | 1.76e-1 |
| FNO (DeltaPhi) | 6.91e-2 | 1.13e-1 | 1.33e-1 | 1.53e-1 | 4.91e-2 | 9.37e-2 | 1.15e-1 | 1.57e-1 |
| Relative Gain | 5.13% ↑ | 5.06% ↑ | 10.43% ↑ | 10.08% ↑ | 27.04% ↑ | 15.65% ↑ | 14.29% ↑ | 10.31% ↑ |
| FFNO (Previous) | 6.64e-2 | 1.04e-1 | 1.24e-1 | 1.43e-1 | 4.89e-2 | 1.01e-1 | 1.27e-1 | 1.49e-1 |
| FFNO (DeltaPhi) | 6.34e-2 | 9.90e-2 | 1.18e-1 | 1.36e-1 | 4.42e-2 | 9.00e-2 | 1.12e-1 | 1.35e-1 |
| Relative Gain | 4.53% ↑ | 5.06% ↑ | 4.84% ↑ | 5.09% ↑ | 9.48% ↑ | 10.72% ↑ | 11.94% ↑ | 9.29% ↑ |

Performance comparison. Table 4 presents the resolution generalization results. Compared to FNO [2], FFNO [11] shows prefer generalization ability for its less number of network weights. In all experimental settings, the proposed physical residual models (tagged with "DeltaPhi") evidently outperform their counterpart base models. The performance improvement of residual operator learning is more noticeable when the training set size is 900. In this setting, FNO (DeltaPhi) managed to match, or even surpass FFNO [11] on resolution 85×85 , 43×43 , and 22×22 , despite using the relatively weaker base network. The results empirically draw the conclusion that physical residual learning improves zero-shot resolution generalization performance.

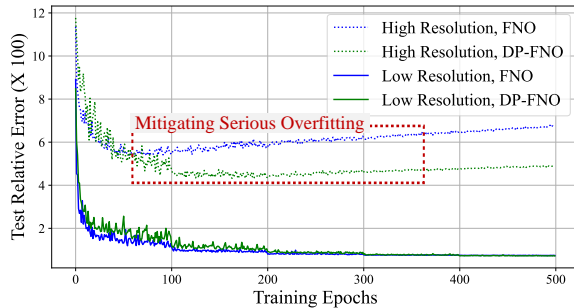


Figure 3: Training curve comparison. "DP-*" denotes the proposed residual learning version of base models.

Training curve comparison. We also report the test loss curve during training in Figure 3. The training data is 900 and the training resolution is 85×85 . As the training proceeds, the relative error on resolution 85×85 data continues to decline. However, after some epochs, the loss on resolution 421×421 gradually increases due to overfitting. The proposed physical residual operator (named with DP-FNO) significantly mitigates this overfitting tendency of the base model (named with FNO).

4.3 Statistical Analysis of Residual Operator Learning

This section further validates the generalization property of DeltaPhi through statistical analysis.

Similarity between output functions. We statistically validate the assumption (mentioned in Section 3.2.5) that the similarities between the input function pair and the corresponding output function pair are positively related. This means that for input function $a^{test}(x)$, the higher similarity score of the auxiliary sample $(a_{k_t}(x), u_{k_t}(x))$, the lower difference between the targeted solution function $u^{test}(x)$ and auxiliary solution function $u_{k_t}(x)$.

In Figure 4, we visualize the variation curve of the normalized distance between $u^{test}(x)$ and $u_{k_t}(x)$ as the similarity rank of $a_{k_t}(x)$ increases on Darcy Flow. (Appendix D.1 presents the visualization details.) The normalized distance consistently increases as the similarity rank increases across different retrieval set size. This result concludes that the similarity between output function pair is positively correlated with the similarity between input function pair, thus the training label distribution could be effectively controlled for alleviating the training label distribution bias.

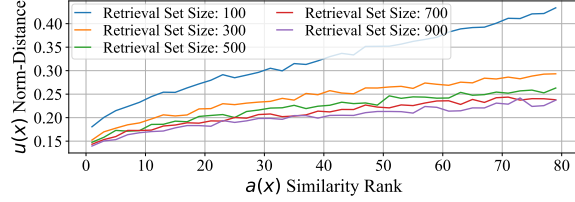


Figure 4: The variation curve of the normalized distance between $u^{test}(x)$ and $u_{k_t}(x)$ as retrieval similarity rank increases. Different color corresponds to different retrieval set sizes.

Training label distribution comparison. Through training label distribution visualization, we statistically validate the enhanced generalization property of DeltaPhi on Darcy Flow. We process both the training dataset and the testing dataset with the following steps. First, the high-dimensional labels (output function) are compressed into 2 dimensions. Then we plot the 2D point of every label and the circles of standard deviation and range for all samples. Appendix D.2 presents more details.

Figure 5 presents the visualization results. (1) As depicted in the left part of Figure 5, in direct operator learning the restricted amount of training data leads to the limited diversity of training labels. Consequently, it is challenging to comprehensively cover the distribution of testing labels with training labels. We refer to this situation as training label distribution bias. In such scenarios, the trained neural operator models struggles with managing certain solutions to be solved. (2) As depicted in the right part of Figure 5, compared to direct operator learning, the testing label distribution becomes more concentrated, and the training labels distribution becomes more dispersed in residual operator learning. The distribution bias between training labels and testing labels is mitigated as mentioned in Section 3.2.5.

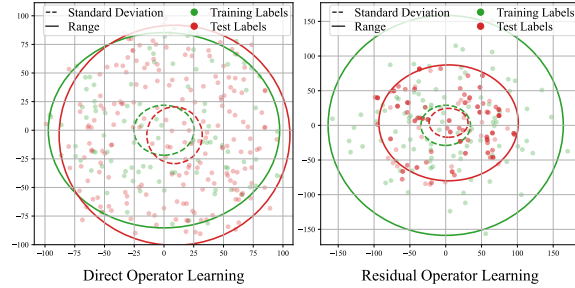


Figure 5: Label distribution visualization on Darcy Flow. The points represent dimension-reduced labels ($u_*(x)$ for direct learning, $u_*(x) - u_{k_*}(x)$ for residual learning) through Principle Component Analysis. The ellipses with dotted lines and solid lines represent the standard deviation and range, respectively. Green and red color correspond to training set and testing set, respectively.

5 Conclusion

This work proposes to learn physical trajectory residuals for PDE solving based on existing neural operator networks. Extensive experiments substantiate that learning residual operator mapping is preferred compared to previous learning direct operator mapping between input-output function fields. We hope the introduced method provides insights for future development of machine learning based PDE solving or other high-dimensional regression problems. In future work, we will explore employing DeltaPhi in practical scenarios of data deficiency and bias, *e.g.* realistic physical phenomenon forecasting, or high-fidelity physics dynamic modeling.

6 Limitation

Despite the comprehensive validation of the superiority of Physical Residual Operator Learning through an extensive range of experiments, we recognize some inherent limitations that, nevertheless, do not impact the solidity of our conclusions. First, when the correlation between the input and output functions of PDEs is weak, such as in chaotic systems, the performance enhancement of the current implementation may be constrained. Second, compared to direct operator learning, the proposed residual operator learning increases the learning difficulty, thus requiring the base model to have sufficient representation capability. Although beyond the scope of this work, these aspects warrant further exploration in future studies.

References

- [1] Nikola Kovachki, Zongyi Li, Burigede Liu, Kamyar Azizzadenesheli, Kaushik Bhattacharya, Andrew Stuart, and Anima Anandkumar. Neural operator: Learning maps between function spaces. *arXiv preprint arXiv:2108.08481*, 2021.
- [2] Zongyi Li, Nikola Kovachki, Kamyar Azizzadenesheli, Burigede Liu, Kaushik Bhattacharya, Andrew Stuart, and Anima Anandkumar. Fourier neural operator for parametric partial differential equations. *arXiv preprint arXiv:2010.08895*, 2020.
- [3] Lu Lu, Pengzhan Jin, and George Em Karniadakis. Deeponet: Learning nonlinear operators for identifying differential equations based on the universal approximation theorem of operators. *arXiv preprint arXiv:1910.03193*, 2019.
- [4] Maziar Raissi, Paris Perdikaris, and George E Karniadakis. Physics-informed neural networks: A deep learning framework for solving forward and inverse problems involving nonlinear partial differential equations. *Journal of Computational Physics*, 378:686–707, 2019.
- [5] Zichao Long, Yiping Lu, Xianzhong Ma, and Bin Dong. Pde-net: Learning pdes from data. In *International conference on machine learning*, pages 3208–3216. PMLR, 2018.
- [6] Zongyi Li, Nikola Kovachki, Kamyar Azizzadenesheli, Burigede Liu, Kaushik Bhattacharya, Andrew Stuart, and Anima Anandkumar. Neural operator: Graph kernel network for partial differential equations. *arXiv preprint arXiv:2003.03485*, 2020.
- [7] Zongyi Li, Hongkai Zheng, Nikola Kovachki, David Jin, Haoxuan Chen, Burigede Liu, Kamyar Azizzadenesheli, and Anima Anandkumar. Physics-informed neural operator for learning partial differential equations. *arXiv preprint arXiv:2111.03794*, 2021.
- [8] Ricardo Vinuesa and Steven L Brunton. Emerging trends in machine learning for computational fluid dynamics. *Computing in Science & Engineering*, 24(5):33–41, 2022.
- [9] Florent Bonnet, Jocelyn Mazari, Paola Cinnella, and Patrick Gallinari. Airfrans: High fidelity computational fluid dynamics dataset for approximating reynolds-averaged navier–stokes solutions. *Advances in Neural Information Processing Systems*, 35:23463–23478, 2022.
- [10] Gengxiang Chen, Xu Liu, Qinglu Meng, Lu Chen, Changqing Liu, and Yingguang Li. Learning neural operators on riemannian manifolds. *arXiv preprint arXiv:2302.08166*, 2023.
- [11] Alasdair Tran, Alexander Mathews, Lexing Xie, and Cheng Soon Ong. Factorized fourier neural operators. *arXiv preprint arXiv:2111.13802*, 2021.
- [12] Zitong Yang, Michal Lukasik, Vaishnavh Nagarajan, Zonglin Li, Ankit Singh Rawat, Manzil Zaheer, Aditya Krishna Menon, and Sanjiv Kumar. Resmem: Learn what you can and memorize the rest. *arXiv preprint arXiv:2302.01576*, 2023.
- [13] Chen Xu and Yao Xie. Sequential predictive conformal inference for time series. In *International Conference on Machine Learning*, pages 38707–38727. PMLR, 2023.
- [14] Yulun Zhang, Yapeng Tian, Yu Kong, Bineng Zhong, and Yun Fu. Residual dense network for image super-resolution. In *Proceedings of the IEEE conference on computer vision and pattern recognition*, pages 2472–2481, 2018.
- [15] Yoav Freund and Robert E Schapire. A decision-theoretic generalization of on-line learning and an application to boosting. In *European conference on computational learning theory*, pages 23–37. Springer, 1995.
- [16] Johannes Brandstetter, Rianne van den Berg, Max Welling, and Jayesh K Gupta. Clifford neural layers for pde modeling. *arXiv preprint arXiv:2209.04934*, 2022.
- [17] Zongyi Li, Miguel Liu-Schiaffini, Nikola Kovachki, Burigede Liu, Kamyar Azizzadenesheli, Kaushik Bhattacharya, Andrew Stuart, and Anima Anandkumar. Learning dissipative dynamics in chaotic systems. *arXiv preprint arXiv:2106.06898*, 2021.

- [18] Michael Poli, Stefano Massaroli, Federico Berto, Jinkyoo Park, Tri Dao, Christopher Ré, and Stefano Ermon. Transform once: Efficient operator learning in frequency domain. *Advances in Neural Information Processing Systems*, 35:7947–7959, 2022.
- [19] Colin White, Renbo Tu, Jean Kossaifi, Gennady Pekhimenko, Kamyar Azizzadenesheli, and Anima Anandkumar. Speeding up fourier neural operators via mixed precision. *arXiv preprint arXiv:2307.15034*, 2023.
- [20] Md Ashiqur Rahman, Zachary E Ross, and Kamyar Azizzadenesheli. U-no: U-shaped neural operators. *arXiv preprint arXiv:2204.11127*, 2022.
- [21] Boris Bonev, Thorsten Kurth, Christian Hundt, Jaideep Pathak, Maximilian Baust, Karthik Kashinath, and Anima Anandkumar. Spherical fourier neural operators: Learning stable dynamics on the sphere. *arXiv preprint arXiv:2306.03838*, 2023.
- [22] Zongyi Li, Daniel Zhengyu Huang, Burigede Liu, and Anima Anandkumar. Fourier neural operator with learned deformations for pdes on general geometries. *arXiv preprint arXiv:2207.05209*, 2022.
- [23] Zhongkai Hao, Zhengyi Wang, Hang Su, Chengyang Ying, Yinpeng Dong, Songming Liu, Ze Cheng, Jian Song, and Jun Zhu. Gnot: A general neural operator transformer for operator learning. In *International Conference on Machine Learning*, pages 12556–12569. PMLR, 2023.
- [24] Ziyuan Liu, Yuhang Wu, Daniel Zhengyu Huang, Hong Zhang, Xu Qian, and Songhe Song. Spfno: Spectral operator learning for pdes with dirichlet and neumann boundary conditions. *arXiv preprint arXiv:2312.06980*, 2023.
- [25] Thomas J Grady, Rishi Khan, Mathias Louboutin, Ziyi Yin, Philipp A Witte, Ranveer Chandra, Russell J Hewett, and Felix J Herrmann. Model-parallel fourier neural operators as learned surrogates for large-scale parametric pdes. *Computers & Geosciences*, page 105402, 2023.
- [26] Shashank Subramanian, Peter Harrington, Kurt Keutzer, Wahid Bhimji, Dmitriy Morozov, Michael Mahoney, and Amir Gholami. Towards foundation models for scientific machine learning: Characterizing scaling and transfer behavior. *arXiv preprint arXiv:2306.00258*, 2023.
- [27] Gaurav Gupta, Xiongye Xiao, and Paul Bogdan. Multiwavelet-based operator learning for differential equations. *Advances in neural information processing systems*, 34:24048–24062, 2021.
- [28] Jiawei Zhao, Robert Joseph George, Yifei Zhang, Zongyi Li, and Anima Anandkumar. Incremental fourier neural operator. *arXiv preprint arXiv:2211.15188*, 2022.
- [29] Qianying Cao, Somdatta Goswami, and George Em Karniadakis. Lno: Laplace neural operator for solving differential equations. *arXiv preprint arXiv:2303.10528*, 2023.
- [30] Tapas Tripura and Souvik Chakraborty. Wavelet neural operator for solving parametric partial differential equations in computational mechanics problems. *Computer Methods in Applied Mechanics and Engineering*, 404:115783, 2023.
- [31] Bogdan Raonic, Roberto Molinaro, Tim De Ryck, Tobias Rohner, Francesca Bartolucci, Rima Alaifari, Siddhartha Mishra, and Emmanuel de Bezenac. Convolutional neural operators for robust and accurate learning of pdes. In *Thirty-seventh Conference on Neural Information Processing Systems*, 2023.
- [32] Johannes Brandstetter, Daniel Worrall, and Max Welling. Message passing neural pde solvers. *arXiv preprint arXiv:2202.03376*, 2022.
- [33] Zongyi Li, Nikola Kovachki, Kamyar Azizzadenesheli, Burigede Liu, Andrew Stuart, Kaushik Bhattacharya, and Anima Anandkumar. Multipole graph neural operator for parametric partial differential equations. *Advances in Neural Information Processing Systems*, 33:6755–6766, 2020.
- [34] Shuhao Cao. Choose a transformer: Fourier or galerkin. *Advances in neural information processing systems*, 34:24924–24940, 2021.

- [35] Michael Prasthofer, Tim De Ryck, and Siddhartha Mishra. Variable-input deep operator networks. *arXiv preprint arXiv:2205.11404*, 2022.
- [36] Jae Hyun Lim, Nikola B Kovachki, Ricardo Baptista, Christopher Beckham, Kamyar Azizzadenesheli, Jean Kossaifi, Vikram Voleti, Jiaming Song, Karsten Kreis, Jan Kautz, et al. Score-based diffusion models in function space. *arXiv preprint arXiv:2302.07400*, 2023.
- [37] Shuohang Wang, Yichong Xu, Yuwei Fang, Yang Liu, Siqi Sun, Ruochen Xu, Chenguang Zhu, and Michael Zeng. Training data is more valuable than you think: A simple and effective method by retrieving from training data. *arXiv preprint arXiv:2203.08773*, 2022.
- [38] Kelvin Guu, Kenton Lee, Zora Tung, Panupong Pasupat, and Mingwei Chang. Retrieval augmented language model pre-training. In *International conference on machine learning*, pages 3929–3938. PMLR, 2020.
- [39] Loh Sher En Jessica, Naheed Anjum Arafat, Wei Xian Lim, Wai Lee Chan, and Adams Wai Kin Kong. Finite volume features, global geometry representations, and residual training for deep learning-based cfd simulation. *arXiv preprint arXiv:2311.14464*, 2023.
- [40] Anastasios N Angelopoulos, Emmanuel J Candes, and Ryan J Tibshirani. Conformal pid control for time series prediction. *arXiv preprint arXiv:2307.16895*, 2023.
- [41] Tobias Pfaff, Meire Fortunato, Alvaro Sanchez-Gonzalez, and Peter W Battaglia. Learning mesh-based simulation with graph networks. *arXiv preprint arXiv:2010.03409*, 2020.
- [42] Kaiming He, Xiangyu Zhang, Shaoqing Ren, and Jian Sun. Deep residual learning for image recognition. In *Proceedings of the IEEE conference on computer vision and pattern recognition*, pages 770–778, 2016.
- [43] Will Hamilton, Zhitao Ying, and Jure Leskovec. Inductive representation learning on large graphs. *Advances in neural information processing systems*, 30, 2017.
- [44] Lu Lu, Xuhui Meng, Shengze Cai, Zhiping Mao, Somdatta Goswami, Zhongqiang Zhang, and George Em Karniadakis. A comprehensive and fair comparison of two neural operators (with practical extensions) based on fair data. *Computer Methods in Applied Mechanics and Engineering*, 393:114778, 2022.
- [45] Pengzhan Jin, Shuai Meng, and Lu Lu. Mionet: Learning multiple-input operators via tensor product. *SIAM Journal on Scientific Computing*, 44(6):A3490–A3514, 2022.
- [46] Diederik P Kingma and Jimmy Ba. Adam: A method for stochastic optimization. *arXiv preprint arXiv:1412.6980*, 2014.

A Ablation Studies

A.1 Influence of Similar Trajectory Retrieval

In this section, we test the impact of different retrieval ranges K presented in Equation (6) under various training data scales.

Setup. The experimental PDEs are Darcy Flow [2] and Navier-Stokes [2]. We randomly sample 100, 300, 500, 700, and 900 data for training, and evaluate the trained models on an additional 200 test data with the same resolution. FNO [2] and Resnet [42] are included as the base model for comparison. Besides, we experiment with varying retrieval range K on different training data scales and evaluate the performance without utilizing *Similar Trajectory Retrieval*.

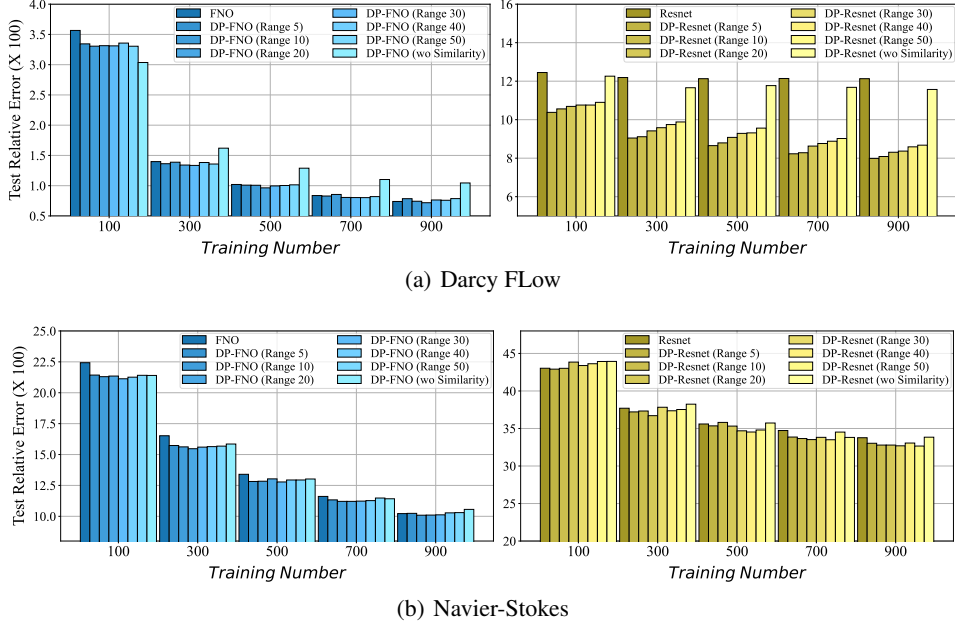


Figure 6: Influence of similar trajectory retrieval range K (presented in Equation (6)). "DP-*" denotes the proposed residual learning version of each base model.

Performance Comparison. The experimental results are shown in Figure 6. In most settings, the physical trajectory residual learning framework DP-FNO and DP-Resnet outperform their corresponding baselines FNO [2] and Resnet [42] respectively. In the small data regime, this performance enhancement is particularly evident. Additionally, on Darcy Flow in Figure 6(a), as the amount of training data increases, the performance increasing of the weak base model Resnet [42] gradually converges, while the corresponding residual operator DP-Resnet continually improves. Same as Table 3, the experimental results validate that the proposed residual operator learning performs better across various training set scales, especially on small data scenarios.

Influence of Similar Trajectory Retrieval. Figure 6 presents the physical residual learning with varying similar trajectory retrieval range K , as well as the simply random sampling without considering similarity (could also be seen as setting K as the training set size). On various settings, as the sampling similarity range K increases, the overall trend is that the model's performance first rises and then falls. This suggests that setting an appropriate range K is of significant importance. Another point worth noting is that, in nearly all settings, the model's performance appears to be the poorest when similarity-based retrieval is removed. This demonstrates the crucial role of Similar Trajectory Retrieval. These experimental results lead to the conclusion that Similar Trajectory Retrieval plays an important role in the physical residual learning framework.

A.2 Customized Auxiliary Input Ablation

This section conducts ablation experiments on the customized auxiliary input.

Setup. We evaluate the influence of customized auxiliary input on Navier-Stokes. The training trajectory number is 100. FNO [2] is used as the base model. We test 3 types input of $a_{k_i}(x)$, including complete $a_{k_i}(x)$, empty $a_{k_i}(x)$ and partial (last 3 trajectory steps) $a_{k_i}(x)$. In addition, we experiment with the inclusion or omission of $u_{k_i}(x)$, as well as the addition or exclusion of $Score_{i,k_i}$.

Customized Auxiliary Input Influence. The results are shown in Table 5. The first three rows indicate that utilizing partial $a_{k_i}(x)$ yields the best results for $a_{k_i}(x)$. When comparing the third row with the fourth row, or the fifth row with the sixth row, it’s evident that incorporating $Score_{i,k_i}$ is also meaningful. Additionally, when comparing the third row with the fifth row, as well as the fourth row with the sixth row, the inclusion of $u_{k_i}(x)$ proves to be extremely crucial. The above findings suggest that the utilization of customized input is beneficial, thereby confirming the conclusion that proper customized input could improve performance.

A.3 Auxiliary Trajectory Selection during Inference

As described in Section 3.2.2, we greedily select take the auxiliary sample with the top similarity score during inference. To validate the robustness of the trained residual neural operator on different auxiliary samples, we experiment with randomly sampled auxiliary trajectories from the top-10 similarity scores. The experiment is conducted on Darcy Flow with FNO as the base model.

Table 6 presents the relative error of every experimental run and the standard deviation (STD) across five repeated experiments. The low standard deviation value **5.41e-5** indicates that the trained residual neural operators are not sensitive to the selection of auxiliary samples. This concludes that the neural operator effectively learns the proposed residual operator mapping.

A.4 Different Similarity Function

We use Cosine Similarity for its two advantages:

- Unaffected by the magnitude of the numerical value. Thus it could be conveniently applied to various PDEs without considering the numerical scale distribution of physical fields.
- Taking normalized values in $[0, 1]$. We could simply use it as an additional network input. As Table 5 shows, incorporating the similarity scores improves the model’s performance on the Navier-Stokes equation.

To explore more retrieval metrics for scientific machine learning, we experiment with other discrepancy metrics (all the distance values are calculated after normalization), as shown in Table 7. The results indicate that different distance functions yield subtle impacts. Euclidean Distance and Manhattan Distance are also appropriate choices. Additionally, inspired by the great success of the NLP community, conducting retrieval in the latent space may yield superior results. We will explore this in the next step.

Table 5: Ablation of customized auxiliary input on Navier-Stokes. **Bold font**, underline and wavyline respectively denote the best, second best, and inferior results.

| Customized Auxiliary Input | | | Relative Error |
|----------------------------|--------------|-----------------|----------------|
| $a_{k_i}(x)$ | $u_{k_i}(x)$ | $Score_{i,k_i}$ | |
| All | ✓ | ✓ | 2.14e-1 |
| X | ✓ | ✓ | 2.20e-1 |
| Partial | ✓ | ✓ | 2.13e-1 |
| Partial | ✓ | | <u>2.13e-1</u> |
| Partial | | ✓ | <u>2.34e-1</u> |
| Partial | | | <u>2.37e-1</u> |

Table 6: Results of repeat Evaluation using random auxiliary sample with Top-10 similarity score.

| Relative Error of FNO (DeltaPhi) | |
|----------------------------------|--------------|
| Infer 1 | 3.3441876e-2 |
| Infer 2 | 3.3364178e-2 |
| Infer 3 | 3.3501464e-2 |
| Infer 4 | 3.3489122e-2 |
| Infer 5 | 3.3489122e-2 |
| STD | 5.40649e-5 |

Table 7: Results of DeltaPhi-FNO using different similarity function.

| Similarity Functions | Relative Error |
|----------------------|----------------|
| Cosine Similarity | 3.31e-2 |
| Euclidean Distance | 3.31e-2 |
| Manhattan Distance | 3.28e-2 |

B Experimental Detail

B.1 Dataset

B.1.1 Regular Domain

Darcy Flow. Darcy Flow is a steady-state solving problem. We conduct the experiment on Darcy Flow using the same dataset as [2], consisting of 421×421 resolution fields with Dirichlet boundary. The low resolution data *e.g.* 22×2 are obtained via uniformly downsampling operation.

Navier-Stokes. Navier-Stokes is a challenging time-series solving problem. We use the public dataset from [2]. The viscosity of trajectories is $1e - 5$ ($Re = 2000$). The spatial resolution is 64×64 . The input and output time step length are both 10.

B.1.2 Irregular Domain

For these irregular domain problems, we take the exactly same setting with NORM, more details about the dataset can be found in [10].

Irregular Darcy. The irregular Darcy problem is to solve the Darcy Flow equation defined on an irregular domain. The input function $a(x)$ represents the diffusion coefficient field and the output function $u(x)$ is the corresponding pressure field. The domain is represented with a set of triangle meshes consisting of 2290 nodes. Following [10], we train the neural operators with 1000 data and test them on additional 200 trajectories.

Pipe Turbulence. Pipe Turbulence is a dynamic fluid system described by the Navier-Stokes equation. The computational domain is an irregular pipe shape represented as 2673 triangle mesh nodes. In this problem, the neural operator is required to predict the velocity field in the next frame given the previous velocity field. Same as [10], 300 trajectories are employed for training, and 100 data are used for evaluation in our experiments.

Heat Transfer. In the Heat Transfer problem, the energy transfer phenomena due to temperature difference is studied. The system evolves under the governing law described by the Heat equation. The neural operator is optimized to predict the 3-dimensional temperature field in 3 seconds given the initial boundary temperature state. The output physical domain is represented by triangle meshes with 7199 nodes. We use 100 data for training and the rest of 100 data for evaluation.

Composite. Composite problem is to predict the deformation field in high-temperature stimulation, which is greatly significant for composites manufacturing. The learned operator is expected to predict the deformation field given the input temperature field. Following [10] The studied geometry in this work is an air-intake structural part of a jet, which is composed of 8232 nodes. The training data size is 400 and the test data size is 100.

Blood Flow. This problem aims to predict blood flow in the aorta, which contains 1 inlet and 5 outlets. The blood flow is simulated as a homogeneous Newtonian fluid. The computational domain is completely irregular and represented by a set of triangle meshes comprising 1656 nodes. The simulated temporal length is 1.21 seconds with the temporal step length of 0.01 seconds. The neural operator predicts the velocity field at different times given the velocity boundary at the inlet and pressure boundary at the outlet. In this problem, we have 400 data for training and 100 data for testing, same as [10].

B.2 Base Model

Fourier Neural Operator (FNO) [2]. Fourier Neural Operator (FNO) [2] utilizes the Fourier Transform based integral operation to implement the neural operator kernel \mathcal{K}_i . We implement the FNO with the officially published code under the up-to-date deep learning framework. All model hyperparameters except the hidden channel width (64 in our experiment, 32 in the original implementation) are kept the same as in the original manuscript. The incremental hidden channels enhance the model’s representation capability, obtaining consistent performance improvement in all settings. The optimization setup (Adam [46] optimizer with initial learning rate 0.001 and weight decay 0.0001, StepLR scheduler with step size 100 and $\gamma = 0.5$) is consistent with official implementation.

Factorized Fourier Neural Operator (FFNO) [11]. Factorized Fourier Neural Operator (FFNO) [11] conducts the Fourier Transform along every dimension independently, reducing the model size and enabling deep layer optimization. We implement FFNO via the independent Fourier Transform along each dimension, the improved residual connections, and the FeedForward-based encoder-decoder. All model hyperparameters and optimization setups are consistent with FNO.

Clifford Fourier Neural Operator (CFNO) [16]. Clifford Fourier Neural Operator (CFNO) [16] employs the Clifford Algebra in the neural network architecture, incorporating geometry prior between multiple physical fields. We employ the official implementation for the model architecture. The signature is set as $(-1, -1)$ and we pad lacked physical channels with zero. All hyperparameters except the channel width (32 in CFNO) remain consistent with FNO. The training setup (including the optimizer and scheduler) is the same as FNO.

Galerkin [34]. Galerkin proposes to learn the neural operator with linear attention. We employ the same model architecture as the original work. The network depth is 4, the head number in the attention layer is set as 2, and the latent dimension in the feedforward layer is 256. We use the Galerkin attention mechanism and set the dropout value as 0.05. In our experiment, we use the same training setup as FNO.

GNOT [23]. GNOT is also an attention-based neural operator structure, which introduces the heterogeneous normalized attention layer to handling various inputs such as multiple system inputs and irregular domain meshes. We employ the official architecture implementation. The network depth is set as 4, the hidden dimension is 64, and the activation function is GeLU. The training setup is the same as FNO.

MiOnet [45]. MiOnet [45] is an enhanced version of DeepOnet [3]. It processes multiple inputs by utilizing multiple branch networks and then merging all branch outputs with several fully connected layers. In our implementation, the depth of all branch layers, trunk layer, and merging layer are set as 4. The latent dimension is set as 128. We take the same training setup with FNO.

Resnet [42]. Resnet [42] is a classical network architecture in image processing. Although it fails in zero-shot resolution generalization inference for learning infinite dimension operator mapping, the powerful capability of capturing local details deserves attention. We implement Resnet by simply replacing the spectral convolution in FNO with 3×3 spatial convolution operation. All model hyperparameters and optimization setups remain consistent with FNO.

B.3 Implementation Details

Except for specific statements, the experimental details are as follows:

- Retrieval: For training, the auxiliary trajectory retrieval range K is set as 20. During inference, the auxiliary trajectory with the most similarity with a_i is retrieved.
- Input: The customized input function is partial (last 3 channels) a_{k_i} and complete u_{k_i} .
- Optimizing: We use the Adam [46] optimizer with initial learning rate 0.001 and weight decay 0.0001. The StepLR scheduler with step size 100 and $\gamma = 0.5$ is used to control the learning rate. The batch size is set as 8. All models are trained for 500 epochs. All experiments could be conducted on a single NVIDIA GeForce RTX 4090 device.

B.4 Metric

The evaluated metric is Relative L2 Error, defined as:

$$L2 = \frac{1}{N} \sum_{i=1}^N \frac{\|\hat{u}_i - u_i\|_2}{\|u_i\|_2}, \quad (12)$$

where \hat{u}_i and u_i are predicted trajectory and real trajectory respectively.

C Additional Method Detail

C.1 Selection of K Value

The optimal value of K is hard to determine. It depends on the generalization problem type (limited training data problem and resolution generalization problem in this work), the base models, etc. Empirically, the larger the value of K , the better the model’s generalization range, but the learning difficulty also increases. A proper value of K should ensure enough diversity of training residuals for generalizing to the targeted pending solved physical trajectories. Thus, it is advisable to set a larger K value when the discrepancy between the training set and test set is evident, and the model’s representation ability is considerably strong. Through extensive experiments, we find $K = 20$ is an applicable value for the focused generalization problem of this work, ie. the limited amount and resolution of training data.

For more challenging generalization problems (eg. serious data bias problems in realistic scenarios), we provide an empirical selection algorithm for the "initial value" decision of K (the "final value" of K is also related to the base model’s capability). Given the training set (noted as $\{a_i^{train}\}_{i=1}^{N_{train}}$), suppose the input functions (noted as $\{a_i^{test}\}_{i=1}^{N_{test}}$) of pending solved physical trajectories is available. The initial value of K could be calculated with the following steps: (1) Retrieve the most similar trajectory (noted as $\{a_{k_i}^{test}\}_{i=1}^{N_{test}}$) from the training set for every pending solving function. We denote the similarity values between a_i^{test} and $a_{k_i}^{test}$ as s_i^{test} . (2) Calculate the maximum value s_{max}^{test} of $\{s_i^{test}\}_{i=1}^N$. (3) For every training trajectory a_i^{train} , calculate its similarity with other training trajectories. Denote the index of r -th similar trajectory with a_i^{train} as k_i^r , and the similar score between a_i^{train} and $a_{k_i^r}^{train}$ as s_i^r . (4) The K is calculated as the minimum r satisfying $s_{max}^{test} \leq s_i^r$ for any $i \in [1, N^{train}]$.

C.2 Variant Resolution Auxiliary Trajectory Integration

Sometimes the auxiliary function a_{k_i} has a different resolution. For example, when we need to predict high-resolution physical trajectory using low-resolution trained models, the auxiliary samples a_{k_i} in the training set are more coarse-grained than the queried function a^H . In this scenario, we could interpolate the low-resolution auxiliary sample to a fine-grained grid, then concatenate the interpolated high-resolution grid with the queried function a_i^H .

$$a_{input} = \mathcal{F}^{inter}(a_{k_i}) \oplus a^H. \quad (13)$$

In this work, we implement the interpolation method \mathcal{F}^{inter} based on the Fourier Transform. Specifically, we first transform the coarse-grained input u_{k_i} into Fourier Space, fill zeros in the high-frequency region to target resolution, and finally transform it back to spatial space. Our experimental results show the trained residual neural operator could generalize well in this interpolation scenario.

C.3 Variant Resolution Trajectory Retrieval

For the high resolution inference scenario, we could first downsample the high-resolution queried function a^H to low resolution a_{low}^H , then calculate the similarity score:

$$\begin{aligned} \mathcal{F}^{ret}(a^H, \mathcal{T}) &= \operatorname{argmax}_j \operatorname{Sim}(a_{low}^H, a_j), \\ a_{low}^H &= \mathcal{F}^{low}(a^H), \end{aligned} \quad (14)$$

where \mathcal{F}^{low} is down sampling function. In this work, we implement \mathcal{F}^{low} by erasing additional information in high-frequency regions based on the Fourier Transform.

C.4 Complexity Analysis of Physical Trajectory Retrieval

The computational cost for retrieval is negligible compared to neural network inference. Here is a detailed analysis of the computational cost for physical trajectory retrieval.

The computational expensive is mainly related to two factors: the training set size (noted as N_{train}) and the number of physical field points (ie. the resolution of physical field) (noted as N_{field}). The computing process consists of the following two steps:

- Step 1: Similarity Score Calculation. For every sample in the retrieval set, the similarity metric function (eg. Cosine Similarity) could be calculated with linear time complexity $O(N_{field})$. Thus the time complexity of calculating similarity scores for all retrieved samples is $O(N_{field} \cdot N_{train})$.
- Step 2: Ranking based on similarity scores. We use the simple sorting algorithm (Quicksort) to rank all samples based on their similarity score. The time complexity is $O(N_{train} \cdot \log N_{train})$. The overall time complexity for retrieval is $O(N_{field} \cdot N_{train} + N_{train} \cdot \log N_{train})$.

Commonly, the numerical ranges for N_{field} and N_{train} are approximately between 10^3 to 10^4 , and 10^2 to 10^4 , respectively. Therefore, the real computational amount is about $O(10^8)$, this could be calculated on most computers. In our implementation, the average retrieval time on Darcy Flow (85×85 resolution) is $2.67\text{e-}3$ to $1.84\text{e-}2$ seconds for different retrieval set sizes (100 to 900).

D Visualization Analysis Detail

D.1 Similarity between $u(x)$ Visualization Detail

We visualize the correlation between $u(x)$ normalized distance and $a(x)$ similarity rank (shown in Figure 4) as following steps: Firstly, taking the training set \mathcal{T} as retrieval set, we sample auxiliary trajectory $(a_{k_{i,r}}, u_{k_{i,r}})$ with r -th top similarity score for every test sample (a_i^{test}, u_i^{test}) in the test set. Here r represents the similarity rank (higher r indicates lower similarity), and we take gradually increasing values from 1 to 80 for r . Next, we calculate the normalized distance between u_i^{test} with its auxiliary sample $u_{k_{i,r}}$. The normalized distance is defined the same as the relative error Equation (14).

D.2 Label Distribution Visualization Detail

We visualize the label distribution (as shown in Figure 5) by reducing the high-dimension function fields to 2 dimensions utilizing Principle Component Analysis. Specifically, for both direct operator mapping and residual operator mapping, we first optimize a PCA model on the training labels (100 labels) and then calculate the dimension-reduced labels for every trajectory in the training and testing set. Finally, we visualize every two-dimension label point on the graph as well as the ellipses representing the stand deviation and the range along each dimension.